



Lagrangian particle-based simulation of waves: a comparison of SPH and PFEM approaches

Nicolò Salis¹ · Alessandro Franci^{2,3} · Sergio Idelsohn^{2,4} · Alessandro Reali^{1,5} · Sauro Manenti^{1,5}

Received: 26 February 2023 / Accepted: 24 April 2023 / Published online: 11 May 2023
© The Author(s) 2023

Abstract

Lagrangian numerical methods are particularly suitable to reproduce flows involving large and rapid deformation of the domain, fluid splitting and coalescence, jets and sprays. The absence of the convective terms in the governing equations avoids numerical diffusion. This paper provides a comparative study between two Lagrangian particle models based on the Smoothed Particle Hydrodynamics (SPH) and the Particle Finite Element Method (PFEM). The description of the methods is provided; features and drawbacks of each method are compared and discussed. The introduced models, which represent widely used advanced analysis tools, are compared and validated in the simulation of five test cases: Two solitary waves, two regular wave trains and a non-linear wave-structure impact. Results from each model are similar and quite close to reference data. Therefore, both models have been validated against new test cases never simulated before, showing that these models can be effectively used for the analysis of regular and non-linear wave with structure impact.

Keywords SPH · PFEM · Particle methods · Solitary waves · Regular waves · Non-linear waves · Breaking waves

1 Introduction

Extreme wave events are of great concern in coastal and ocean engineering. Furthermore, these events are expected to grow in number and severity owing to climate change. Wave-structure impacts may cause severe damages to offshore and coastal structures, besides causing human and economic losses. Moreover, bores that may originate can be highly risky for seaside urban areas. Numerical simulation can be of strategic relevance to predict the effects of wave-structure impact. With the recent developments in computational capabilities, simulations are much faster, cheaper and

more accessible than an experimental campaign. Moreover, numerical simulation allows the investigation of several test configuration with relative ease. Furthermore, numerical methods allow a full-scale simulation of a real event thus overcoming scale effect-induced problems, though they may need to be validated with the aid of experimental or field data. Numerical wave generation and wave-structure interaction, although widely investigated in literature with both Eulerian and Lagrangian strategies, still represent a challenging task. On the one hand, Eulerian methods need an *ad-hoc* treatment for dealing with evolving free-surface, such as the use of Level Set functions, and may suffer from numerical diffusion in the simulation of advection-dominated flows. Despite these inconveniences, Eulerian methods have been successfully employed for the generation of regular waves [1, 2], solitary and non-linear waves [3, 4] and wave-structure interaction [5, 6]. On the other hand, Lagrangian strategies allow for a natural tracking of the deforming fluid domain and modelling of the convective term. However, in mesh-based Lagrangian methods, the progressive deterioration of the mesh limits the application of these methods to small deformation problems. Lagrangian particle methods overcome this limitation either by avoiding the use of the mesh, such as in the Smoothed Particle Hydrodynamics (SPH) method [7], or by combining the use of material

✉ Nicolò Salis
nicolo.salis01@universitadipavia.it

¹ Department of Civil Engineering and Architecture DICAr, University of Pavia, 27100 Pavia, Italy

² International Center for Numerical Methods in Engineering, (CIMNE), 08034 Barcelona, Spain

³ Universitat Politècnica de Catalunya, (UPC), 08034 Barcelona, Spain

⁴ Institució Catalana de Recerca i Estudis Avançats, (ICREA), 08034 Barcelona, Spain

⁵ Water Research Center CRA, University of Pavia, 27100 Pavia, Italy

particles with a fixed solving mesh, such as in the Material Point Method (MPM) [8] or in the Particle Finite Element Method of second generation (PFEM-2) [9], or by using an efficient remeshing procedure, such as in the Particle Finite Element Method (PFEM) [10].

In this comparative analysis, we focus our attention on the application to wave generation and structure impact of two particle-based methods, namely the SPH and the PFEM.

The SPH was introduced in [7, 11] to solve astrophysical problems. Subsequently, it has been also adapted to simulate continuum solid and fluid mechanics problems [12, 13] along with alternative methods, such as the Moving Particle Method (MPS) [14], the Consistent Particle Method [15] and the Incompressible SPH [16]. Applications of the SPH to wave propagation and fluid–solid interaction can be found in [17–21]. In this work, we will use the weakly-compressible SPH formulation presented in [20].

Since its pioneering works [10, 22], the PFEM has been applied to complex fluid dynamics problems in presence of free-surface flows and fluid–structure interaction phenomena. Previous PFEM works in the context of wave propagation problems can be found in [23–25]. In more recent publications [26, 27], complex fluid–structure interaction phenomena involving strong wave impact and structural failure were also considered. In this work, we will use the weakly-compressible PFEM formulation presented in [28].

SPH and PFEM have some common features. Both numerical techniques are classified as particle methods, since they discretise the computational domain into a discrete set of particles that move according to the equation of motion. Despite this continuous nature, both methods allow sprays formation which subsequently splash onto the main water body, thus allowing wave-breaking analysis. However, while the SPH is a mesh-less method, without a connection between particles, the PFEM solution is computed using a FEM mesh. In particular, the SPH embraces the concept of integral representation of functions using a kernel function (Fig. 1(a)) that mimics the Dirac’s delta but is continuous and differentiable. Instead, in the PFEM, a computational mesh is generated using the particles as mesh nodes. Then, after the appropriate definition of shape functions (Fig. 1(b)), this mesh is used for the finite

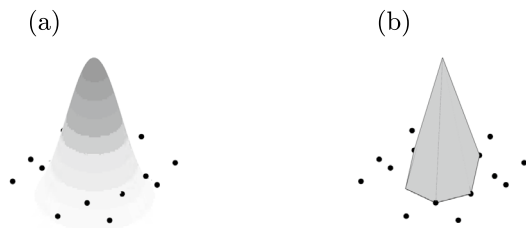


Fig. 1 Graphical representation of SPH kernel (a) and PFEM (FEM) (b) shape functions for a cloud of points

element solution of the Lagrangian governing equations. To circumvent mesh distortion in large-deformation problems, the PFEM regenerates the mesh continuously via an efficient remeshing technique based on a Delaunay triangulation algorithm [29, 30].

In this work, two distinct frameworks are used for the SPH and PFEM solvers. For the SPH solution, is adopted a Free and Open-Source Software (FOSS) derived from SPHERA v.9.0.0 (RSE SpA) by introducing relevant modifications of the research code [31]. Instead, for the PFEM, the formulation implemented in the PfmFluidDynamicsApplication module of the open-source code Kratos Multiphysics [32] is used.

In this work, two models based on SPH and PFEM are applied to the analysis of regular, non-linear and solitary waves with structure impact in two-dimensional flumes. Some of the investigated test cases have never been performed before and represent a validation of these models. To the best of the authors’ knowledge, this document represents the first comparison (and result discussion) between these two particle methods.

The layout of the paper is described in the following. In Sect. 2, the governing equations of the problem are presented. In Sects. 3 and 4, the mathematical models and solution algorithms of the SPH and the PFEM are briefly described. In Sect. 5, the models are validated on three significant test cases. The first test concerns solitary waves, where simulation results are validated with laboratory results for two different experimental campaigns. These test cases are new for the SPH model. The second test is the generation of regular waves in a flume and the validation with the linear wave theory [33]. The third test represents a non-linear wave impacting on a fixed box-shaped structure validated with experimental results. These last two test cases are new for the PFEM model.

2 Governing equations

The Navier–Stokes equations are solved by both the SPH and the PFEM. In Eqs. (1a) and (1b), the strong form of the governing equations (momentum and mass balance equations, respectively) for a Newtonian fluid are written in an updated Lagrangian framework.

$$\rho \frac{\partial \mathbf{u}}{\partial t} - \nabla \cdot \left(2\mu \left(\frac{1}{2} (\nabla \mathbf{u} + \nabla \mathbf{u}^T) - \frac{1}{3} (\nabla \cdot \mathbf{u}) \mathbf{I} \right) - p \mathbf{I} \right) = \mathbf{b} \quad \text{in } \Omega_t \times (0, \tau) \quad (1a)$$

$$\frac{\partial \rho}{\partial t} + \rho \nabla \cdot \mathbf{u} = 0 \quad \text{in } \Omega_t \times (0, \tau) \quad (1b)$$

Where \mathbf{u} is the velocity vector, p is the pressure, \mathbf{b} is the body force per unit volume, μ is the fluid dynamic viscosity, ρ is the density, t is the time, Ω_t is the updated computational

domain, τ is the total time duration, and \mathbf{I} is the identity second-order tensor. We remark that both the SPH and the PFEM strategies used in this work are based on a quasi-incompressible formulation. We also remark that Eq. (1b) can be re-written by substituting the density with the pressure as follows

$$\frac{\partial p}{\partial t} + \kappa \nabla \cdot \mathbf{u} = 0 \quad \text{in } \Omega_t \times (0, \tau) \tag{2}$$

where κ is the material bulk modulus which is defined as $\kappa = \rho c^2$, being c the speed of sound in the medium. System (1) is complemented by the following boundary conditions

$$\mathbf{u} = \hat{\mathbf{u}} \quad \text{on } \Gamma_v \tag{3a}$$

$$\mathbf{t} = \hat{\mathbf{t}} \quad \text{on } \Gamma_t \tag{3b}$$

being \mathbf{t} the normal projection of the stress tensor on the fluid boundaries, $\hat{\mathbf{u}}$ the prescribed velocities on the Dirichlet boundary (Γ_v), and $\hat{\mathbf{t}}$ the tractions acting on the Neumann boundary (Γ_t), with $\Gamma_v \cup \Gamma_t = \partial\Omega_t$ and $\Gamma_v \cap \Gamma_t = \emptyset$.

3 SPH formulation

The SPH model utilised in this work has been obtained by independently introducing relevant modifications in the original code SPHERA v.9.0.0 (RSE SpA) [31]. This derived code [34] is redistributed on Github (bound to the GNU-GPL license and in respect of SPHERA copyright terms). For a full description of the derived model, the reader is referred to [20]. For further information, interested readers are referred to the documentation of the original SPHERA model [31, 35–38].

3.1 SPH approximation of governing equations

The SPH approximation of the mass balance equation (Eq. (1b)) reads

$$\begin{aligned} \left\langle \frac{d\rho}{dt} \right\rangle_0 &= \sum_b \rho_0 (\mathbf{u}_b - \mathbf{u}_0) \cdot \nabla W \frac{m_b}{\rho_b} \\ &+ 2\rho_0 \int_{V'_h} [(\mathbf{u}_w - \mathbf{u}_0) \cdot \mathbf{n}] \mathbf{n} \cdot \nabla W dx^3 \\ &+ C_s + 2\delta c_0 h \sum_{b=1}^N \psi_{0b} \frac{\mathbf{r}_{0b} \cdot \nabla W}{||r_{0b}||^2} \frac{m_b}{\rho_b} \end{aligned} \tag{4}$$

where the notation “ $\langle \rangle$ ” indicates the SPH particle -discrete-approximation. In this equation the computational particle has subscript 0 while the neighbouring particle has subscript b . ρ is the particle density, m is the particle mass, W is the kernel function and r_{0b} the relative distance between the computational particle and the neighbouring one. \mathbf{n} is the

outward normal vector to the boundary surface, c_0 is the artificial sound celerity, and h is the smoothing length. δ is the diffusive coefficient and ψ_{0b} is the diffusive term formulated accordingly to [39]. The subscripts s and w refer, respectively, to the generic neighbouring surface body particle and the solid boundary [37]. In Eq. (4), the term C_s represents the fluid-body interaction contribution for the mass balance equation and is defined as

$$C_s = 2\rho_0 \sum_s [(\mathbf{u}_s - \mathbf{u}_0) \cdot \mathbf{n}_s] \nabla W_s \varpi_s \tag{5}$$

where ϖ_s is the body particle volume. This scheme first introduced in [40] can be interpreted as a discretisation of the semi-analytic approach. We also remark that the last term of Eq.(4) represents a diffusive contribution that it is needed to obtain a stable pressure field solution [39]. Using the same notation as Eq. (4), the SPH approximation of the momentum balance equation (Eq. (1a)) reads

$$\begin{aligned} \left\langle \frac{d\mathbf{u}}{dt} \right\rangle_0 &= -\mathbf{g} + \frac{1}{\rho_0} \sum_b (p_b + p_0) \nabla W \frac{m_b}{\rho_b} \\ &+ 2 \frac{p_0}{\rho_0} \int_{V'_h} \nabla W dx^3 \\ &- v_m \sum_b \frac{m_b}{\rho_b} \frac{1}{r_{0b}^2} (\mathbf{u}_b - \mathbf{u}_0) \cdot (\mathbf{x}_b - \mathbf{x}_0) \nabla W \\ &- 2 \frac{v_m}{\rho_{0in}} (\mathbf{u}_w - \mathbf{u}_0) \cdot \int_{V'_h} \frac{1}{r_{0w}^2} (\mathbf{x} - \mathbf{x}_0) \nabla W dx^3 \\ &+ \mathbf{a}_s + 2v_0 (\mathbf{u}_w - \mathbf{u}_0) \int_{V'_h} \frac{1}{r} \frac{\partial W}{\partial r} dx^3 \end{aligned} \tag{6}$$

where \mathbf{g} is the gravity acceleration, \mathbf{x} is the position vector of the particle, ρ_{0in} is the initial density of particle 0. The artificial viscosity is defined as $v_m = \rho_{0in} \frac{\alpha h c}{\rho_0}$ where α is the artificial viscosity coefficient ranging between 0.01 and 0.1. Artificial viscosity introduced by [11] bears no relation to real fluid viscosity, while it mimics its behaviour [41]. Moreover, its design allows the simulation of shock phenomena and stabilises the numerical algorithm [42]. For a thorough study on the influence of the artificial viscosity coefficient, the reader is referred to [19, 20].

The term \mathbf{a}_s of Eq.(6) is the fluid-body interaction contribution for the momentum balance equation and is defined as

$$\mathbf{a}_s = \sum_s \left(\frac{p_s + p_0}{\rho_0^2} \right) \nabla W_s m_s \tag{7}$$

we remark that the artificial viscosity term of Eq. (6) has been modified to depend on particle volume instead of mass. This allows to obtain stable simulations of multiphase flows with high density ratio. The system of equations (4) and (6)

is closed by the linearised barotropic equation of state for slightly compressible fluids, which reads

$$p = c_{ref}^2(\rho - \rho_{ref}) + p_0 \quad (8)$$

In SPH, the artificial sound speed c_{ref} must be assumed at least ten times higher than the maximum fluid velocity to guarantee a relative density variation at most equal to 1% [42] and the subscript *ref* stands for the reference state. Concerning the boundary conditions, we remark that no constraints are needed to define the free surfaces. Solid walls are treated with the semi-analytic approach [36] where at the boundaries, the kernel support can partially lie outside the fluid domain. The integral terms in Eqs. (4) and (6) express these boundary contributions. Such terms represent the convolution integral on the portion of the kernel support V'_h that lies outside of the domain and is filled with body particles. A second-order staggered Leapfrog scheme is used to integrate in time the governing equations [38]. The stability criterion for the time integration is given by:

$$dt = \min_0 \left\{ 0.05 \frac{2h^2}{\nu}; CFL \frac{2h}{c_{ref} + |\mathbf{u}|} \right\} \quad (9)$$

Where the utilised viscosity ν is the real fluid viscosity.

3.2 SPH solution scheme

The momentum and the mass balance equations are solved as described below. After the first initialisation of the particles in the domain, i.e., neighbouring search and computations of: \mathbf{r}_{0b} , W , ∇W for the background grid, at each time step the procedure is given by the following steps

1. Evaluation of the integrals for the solid neighbouring surface contour
2. Computation of the momentum balance equation and body dynamics by Eq. (6)
3. Leapfrog integration scheme applied to momentum balance equation
4. Update the particle position (Lagrangian trajectory)
5. Neighbouring search and computations of: \mathbf{r}_{0b} , W , ∇W
6. Evaluation of the integrals for the solid neighbouring surface contour
7. Computation of the mass balance equation (4)
8. Leapfrog integration scheme applied to mass balance equation
9. Pressures computations via the equation of state (8)

4 PFEM formulation

In this work, the PFEM solution is obtained through the velocity-pressure solver for Newtonian fluids presented in [28]. As in standard PFEM formulations, equal order of interpolation (linear) for both the velocity and the pressure unknowns. The Finite Calculus (FIC) stabilisation [28] is adopted to avoid spurious oscillations due to the unfulfillment of the so-called *inf-sup* condition [43]. The formulation is implemented in the open-source code Kratos Multiphysics [32]. In the following sections, the basic features of the method are presented.

4.1 FEM discretisation

In the PFEM, the balance equation system (1) is discretised according to the standard Galerkin Finite Element Method (FEM). The full derivation of the FEM solution scheme is considered out of the scope of this work and only the final discretised, FIC-stabilised form is given.

Following the variational equation approach in [28], the governing equations (1a) and (2) can be written in matrix form as

$$\mathbf{M}_0 \dot{\bar{\mathbf{u}}} + \mathbf{K} \bar{\mathbf{u}} + \mathbf{Q} \bar{\mathbf{p}} = \mathbf{f} \quad (10)$$

$$\mathbf{M}_1 \dot{\bar{\mathbf{p}}} + \mathbf{Q}^T \bar{\mathbf{u}} = \mathbf{S}_\tau \quad (11)$$

where \mathbf{M}_0 is the mass matrix, \mathbf{K} is the viscous matrix, \mathbf{Q} is the gradient matrix, \mathbf{f} is the external force vector, \mathbf{M}_1 is the bulk matrix, and \mathbf{S}_τ includes all terms arising from the FIC stabilisation procedure. The vectors $\bar{\mathbf{u}}$ and $\bar{\mathbf{p}}$ contain respectively the nodal velocities and nodal pressures. The notation $\dot{\bar{\mathbf{a}}}$ stands for the first material derivative of vector $\bar{\mathbf{a}}$. The definition of all the matrices introduced in Eqs. (10) and (11) is provided in appendix A. For the full mathematical development of the discretised equations the reader is referred to [28].

4.2 PFEM solution scheme

At each time step $[{}^n t, {}^{n+1} t]$ of duration Δt , the linear momentum and the mass balance equations are solved iteratively for the nodal velocities and pressures. In the following, the main steps of this implicit PFEM scheme are summarised.

At each non-linear iteration i :

1. Compute the nodal velocities $\bar{\mathbf{u}}^{i+1}$ from Eq.(10)
2. Update the nodal coordinates: ${}^{n+1} \bar{\mathbf{x}}^{i+1}$
3. Compute the nodal pressures $\bar{\mathbf{p}}^{i+1}$ from Eq.(11)

4. Check the convergence: $\frac{\|\bar{u}^{i+1} - \bar{u}^i\|}{\|\bar{u}\|} \leq e_u$,

$$\frac{\|\bar{p}^{i+1} - \bar{p}^i\|}{\|\bar{p}\|} \leq e_p$$

with e_u and e_p prescribed error norms for velocities and pressures.

If condition 4 is not fulfilled, return to 1 with $i \leftarrow i + 1$.

The nodal positions, thus the mesh, are continuously updated in a Lagrangian fashion according to the solution of the governing equations. To maintain a good quality of the discretisation in large deformation problems, such as the ones considered in this work, the mesh is continuously rebuilt. This is done by erasing all the elements of the previous (distorted) mesh but maintaining the nodes. The new mesh is built over this distribution of nodes by combining the Delaunay triangulation [44] and the Alpha-Shape [45] method. The main steps of the PFEM remeshing are summarised in the following.

At each remeshing step:

1. Erase the elements of the previous mesh and maintain the nodes
2. Create a Delaunay triangulation
3. Do Alpha-Shape check to rebuild the boundaries

On one hand, the Delaunay triangulation guarantees a good quality of the elements for the given cloud of nodes, on the other hand, the Alpha-Shape method allows recovering the physical contours of the computational domain with good accuracy. The result is a good-quality mesh ready to be used for the FEM solution of the following computational step. We also remark that in the PFEM, as for the SPH, the fluid-free contours are automatically tracked by the solution algorithm. More details about the PFEM remeshing procedure and its implications on the PFEM solution are provided in [29].

5 Results and discussion

5.1 Solitary waves

Two solitary wave types generated by piston wave-maker are considered for testing the SPH and PFEM models. In Fig. 2, a sketch of the two numerical wave tanks is plotted. For both domains, on the left-hand side there is a piston-type wave-maker. Figure 2 (a) shows the domain for the so-called wave-type A. On the right-hand side of the domain, there are two beaches with a 1:10 slope ratio that are connected by a flat bottom. The wave height is measured at the toe of the upper beach ($x = 90m$) with the gauge *WM*. In the reference laboratory experiments [46], the wave impacted and damaged a

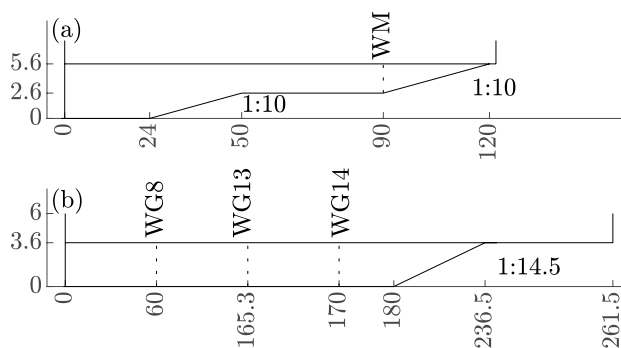


Fig. 2 Numerical wave tanks for solitary waves. **a** Domain for wave-type A [26, 46] **b** domain for wave-type B [27, 47, 48]. In this figure, all measures are in meters

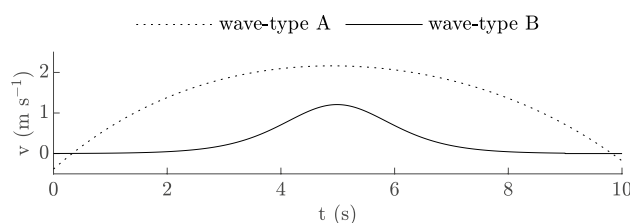


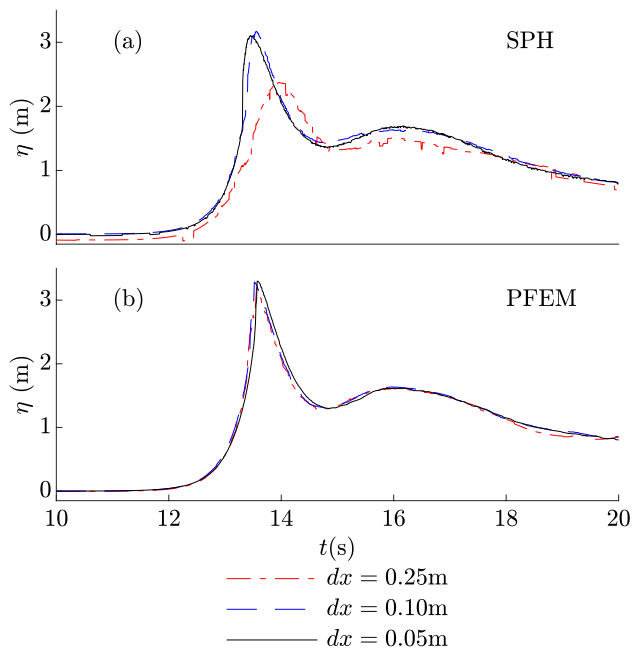
Fig. 3 Velocity input for paddle wave-maker. **a** Solitary wave-type A, **b** solitary wave-type B

reinforced concrete wall that was placed at the right-hand side of the flume. The 3D wave-wall interaction has been fruitfully reproduced with the PFEM method in [26].

Figure 2 (b) shows the domain for wave-type B. This wave type reproduces the laboratory experiment carried out in the large wave flume at the Coastal Research Centre in Hannover [47–49]. At the right-hand side of the domain there is a sloped beach with a 1:14.5 ratio. The sloped beach is followed by a flat part where a bore originates from the solitary wave breaking. The wave height is monitored at three *WG* gauges. This experiment has been reproduced in [27] coupling an Eulerian method and the PFEM method. This is the first attempt to reproduce these wave generation and propagation with SPH. Figure 3 shows the velocity input for the wave-maker for both wave types. While both waves are generated in ten seconds, the propagation in the channel is different: wave-type A propagates in ten seconds while wave-type B propagates in forty seconds. Table 1 shows the spatial resolution and the particle/node number for each wave-type. The wave type is defined in the first column of the table while on the second column the run number is reported to distinguish simulations with different spatial resolution. The third and fourth columns show the particle spacing Δx respectively for the SPH and PFEM model. The fifth column shows

Table 1 Simulation nodes at different resolutions - solitary waves

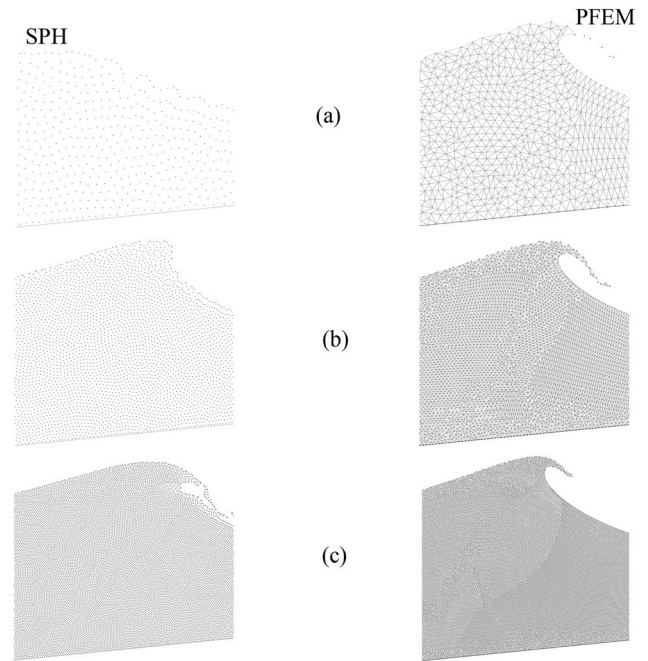
Wave	run	dx (m)		End time (s)	N (-)	
		SPH	PFEM		SPH	PFEM
A	1	0.25	0.25	20.00	6451	8174
A	2	0.1	0.1	20.00	41120	48315
A	3	0.05	0.05	20.00	164480	191661
B	1	0.1	0.1	50.00	75510	88395
B	2	0.05	–	50.00	302040	–

**Fig. 4** Solitary wave-type A: wave elevation at wave gauge WM obtained with spatial discretisation $dx = 0.25\text{ m}$, $dx = 0.1\text{ m}$, and $dx = 0.05\text{ m}$. **a** SPH solution, **b** PFEM solution

the physical simulation end time. On the sixth and seventh columns the particle number (number of nodes) **N** is reported respectively for the SPH and PFEM model.

5.1.1 Solitary wave-type A

This solitary wave, due to the lower particle number and simulation time, is chosen to perform a sensitivity analysis on the particle/mesh size. Table 1 shows the simulation runs where three different spatial resolutions have been considered. Figure 4 shows wave elevation at WM obtained with the SPH and the PFEM models for three different resolutions. These graphs show that the change in resolution has a greater impact on the SPH (Fig. 4 (a)) model than on the PFEM (Fig. 4 (b)). In fact, negligible differences in the wave elevation are exhibited with the PFEM model for the selected mesh sizes. Instead, the wave elevation obtained

**Fig. 5** Solitary wave-type A: domain discretisation at $t = 14.0\text{ s}$. Left-hand panels SPH, right-hand panels PFEM. **a** $dx = 0.25\text{ m}$, **b** $dx = 0.1\text{ m}$, **c** $dx = 0.05\text{ m}$

with the SPH model grows significantly from the coarse to fine resolutions and a very fine mesh is needed to obtain a convergent result. The best result being achieved with the fine spatial resolution. The trough, the second crest and the subsequent descending part of the wave elevation are close to the PFEM model and the experimental wave elevation.

Figure 5 shows a detail of the SPH and PFEM particles/nodes at $t = 14.0\text{ s}$ (wave breaking point) for the three different resolutions. As discussed before, the effect of resolution increase on the numerical results is more significant in the SPH than in the PFEM. Although the number of particles is similar between models (Table 1), at the coarsest resolution (Fig. 5 (a)) the finite element discretisation allows to obtain a more faithful representation of the wave breaking than SPH, and the wave evolves into a plunging breaker. With the middle spatial resolution (Fig. 5 (b)), the accuracy of SPH is greatly improved but the wave breaking is still not so accurately reproduced. At the higher spatial resolution analysed

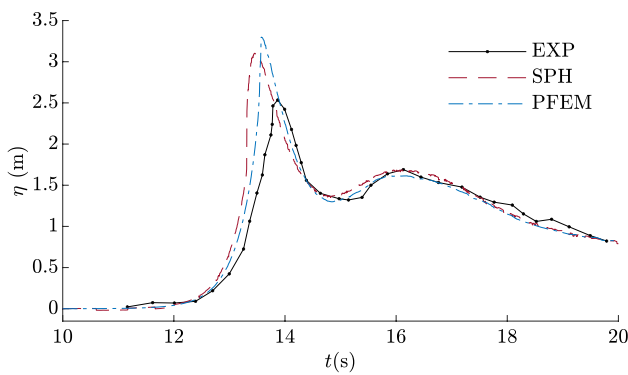


Fig. 6 Solitary wave-type A: wave elevation at wave gauge WM obtained experimentally [46] and numerically with SPH and PFEM

(Fig. 5 (c)) the discretisation is finally sufficient to model the breaking wave with the SPH. Figure 5 also confirms that in the SPH model the wave breaks before the PFEM model. In Fig. 5 (c), the SPH plunging breaker is falling and closing onto the main water body. With the PFEM model, the breaking point is much less influenced by different resolutions. Moreover, the crest gets tighter when resolution increases and with the highest resolution analysed no particles detach from the crest.

Figure 6 shows the wave elevation at WM. Numerical results with the resolution of $dx = 0.05m$ are compared with the experimental results of [46]. The first SPH peak in Fig. 6 is slightly shifted to the left. The SPH wave breaks slightly earlier than the wave generated with the PFEM model. Therefore the first SPH peak is slightly lower than the PFM one. Both models overestimate the experimental peak at 14s. The wave gauge WM is placed at the toe of the upper slope change where the solitary wave becomes a plunging breaker, thus affecting the experimental measure of the wave elevation at the peak. Both models produce a wave profile with negligible differences from the experimental wave. This is particularly evident in the trough and during the descending part of the wave from $t = 14.5s$ to $t = 20s$.

5.1.2 Solitary wave-type B

The original experiment [48] focused on the propagation of the wave in the flat beach and subsequent impact with fixed structures. Based on the previous results, for the PFEM mesh, a resolution coarser than the one adopted for the SPH is used. In particular, with the PFEM, suitable results are achieved with $dx = 0.1m$, while the SPH needs a particle size of $dx = 0.05m$. Even though mesh/particle resolutions are different, the models produce similar results. Figure 7 shows the wave elevation obtained numerically and experimentally at the three gauges WG8, WG13, and WG14. In this figure, two SPH wave

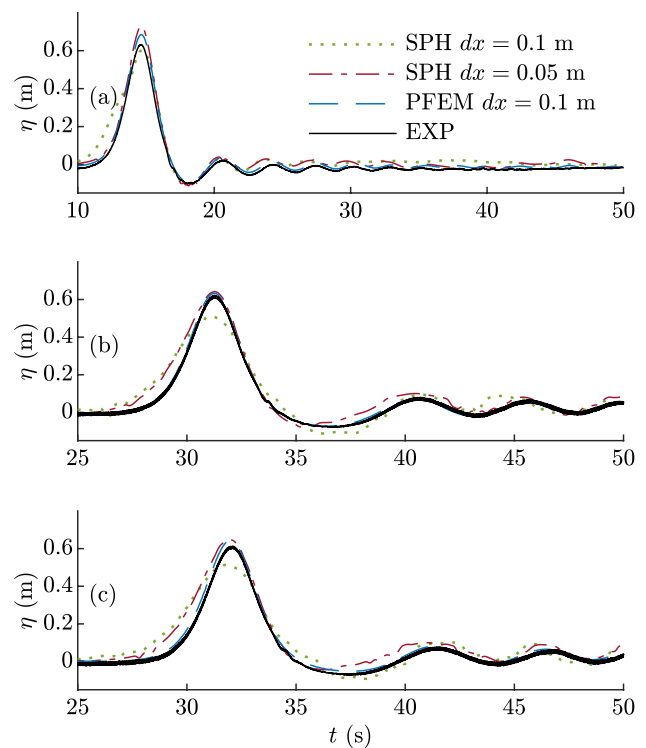


Fig. 7 Solitary wave-type B: wave elevation at sensors: **a** WG8, **b** WG13, **c** WG14 [48]

elevations are shown with $dx = 0.1 m$ and with $dx = 0.05 m$. The first one has the same resolution as the PFEM simulation. As discussed for Fig. 4 at this resolution the SPH model does not converge. Once spatial convergence is achieved by both models (with different discretisation) a fair comparison can be made, showing that results are similar and rather close to the experiment. At WG8, Fig. 7 (a) both models gives a slightly higher wave elevation at the $t = 15.0s$ crest. The models capture the wave train from $t = 18.0s$ to $t = 35.0s$ in both phase and height. For WG13, and WG14, corresponding to Fig. 7 (b) and (c), similar considerations can be made. The wave crest at $t \approx 32.0s$ and the following wave train of smaller amplitude are well estimated with negligible differences between both models and the experiment.

Figure 8 shows the velocity magnitude contour of the solitary wave propagating in the channel. In the PFEM model the highest velocities are centred under the wave crest moving in the channel. In the SPH model, the highest velocities seem diffused in front of and behind the wave crest. The maximum velocity captured at the crest top is $\approx 1ms^{-1}$. Close to the bottom, the SPH velocity is attenuated, while the PFEM contours show higher velocities.

Figure 9 shows the pressure contour. Both models show a quasi hydrostatic distribution, with the PFEM contour

Fig. 8 Solitary wave-type B: velocity magnitude contour at $t = 30.0s$. SPH $dx = 0.05$ m, PFEM $dx = 0.1$ m

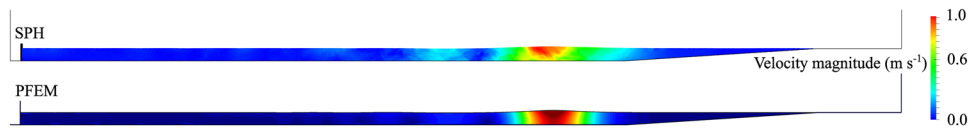


Fig. 9 Solitary wave-type B: pressure contour at $t = 30.0s$. SPH $dx = 0.05$ m, PFEM $dx = 0.1$ m

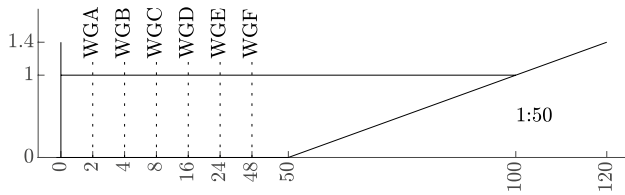
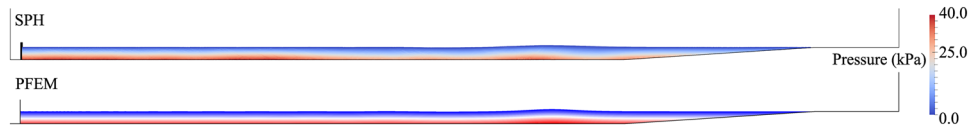


Fig. 10 Numerical wave tank for regular waves. In this figure, all measures are in meters

being slightly more consistent than the SPH one. The pressure increase under the wave crest is detected by both models and is consistent with the increase of free surface height in shallow water.

5.2 Regular waves

The domain is a slight modification of that used in previous SPH simulations [19, 20] to avoid wave reflection due to the sloped beach. Figure 10 shows a sketch of the updated domain, with a milder beach slope 1:50 that allows to reduce wave reflection at measuring gauges. The flat part of the domain has been extended to 50 m. On the left-hand side, there is the piston-type wave-maker. Wave heights are monitored with six wave gauges placed at an increasing distance from the wave-maker with imposed kinematic. This is the first time that the PFEM model is tested on the generation and propagation of regular wave trains in a flume.

Bifsel [50] derived the analytical solution for different wave-maker types. The wave-maker stroke is set to obtain the target wave height. Equation (12) shows the time-velocity law imposed on the wave-maker. S_0 is the maximum displacement (stroke) of the wave-maker, ω is the angular frequency related to the wave period T , and

t is the time variable. The following exponential terms are introduced to avoid inertial effects at early simulation stages:

$$u_x(t) = \frac{1}{2} S_0 \omega \cos(\omega t) \cdot \left(1 - \exp\left(-\frac{t}{T}\right) \right) + \frac{S_0}{2} \sin(\omega t) \cdot \exp\left(-\frac{t}{T}\right) / T \tag{12}$$

The still water height is $h_{still} = 1m$ and is constant in both experiments; wave parameters are obtained with the procedure illustrated in [19, 20]. Two wave types, from Ursell [51] are reproduced. Table 2 summarises the target characteristics of the waves. T is the wave period, H is the wave height, L is the wavelength, S is the maximum paddle stroke, c is the wave celerity, h_{still} is the still water height in the flume, kh is the wave relative depth, H/L is the wave steepness, H/S is the wave height to stroke ratio. One may refer to [19, 20] for a short theoretical description of wave generation. Table 3 shows the adopted dx , the simulation time and the node / particle number for the two models. Figure 11 shows the wave elevation at the wave gauges in the numerical flume for wave-type U15 and U24. Regular wave-types are compared with their respective analytical solution. With both models, the phase and wave heights are accurately reproduced. This numerical flume, with the 1:50 sloped beach, prevents wave reflection. Moreover, this sloped beach prevents mass losses in the PFEM model. In the flat part of the channel both models show negligible wave height reduction with respect to the analytical solution.

Figure 12 (a) shows the magnitude velocity contours for both models at $t = 50s$. The results of the two models are comparable. The velocity at wave crests, troughs, and nodes is well simulated. Slightly lower velocities are obtained with the PFEM model than with the SPH one. It is worth noting that the SPH velocity field is affected by negligible

Table 2 Regular waves characteristics

Wave	T(s)	H (m)	L (m)	S(m)	c (m s ⁻¹)	h_{still} (m)	kh	H/L (-)	H/S (-)
U15	3.01	0.084	8.73	0.12	2.9	1.00	0.72	0.0096	0.7
U24	2.15	0.236	5.76	0.22	2.68	1.00	1.09	0.0409	1.05

Table 3 Simulation nodes - regular waves

Wave	dx (m)		End time (s)	N (-)	
	SPH	PFEM		SPH	PFEM
U15	0.025	0.025	51.0	187500	143325
U24	0.025	0.025	56.0	187500	143325

numerical noise. The dashed box is magnified in Fig. 12 (b) where the velocity vector field under the wave is shown. On the left-hand side, there is the node before the wave crest, where the horizontal component of velocity is null and the vertical component is directed downwards. Under the wave crest the vertical component of velocity is null and the horizontal component is directed along the wave propagation

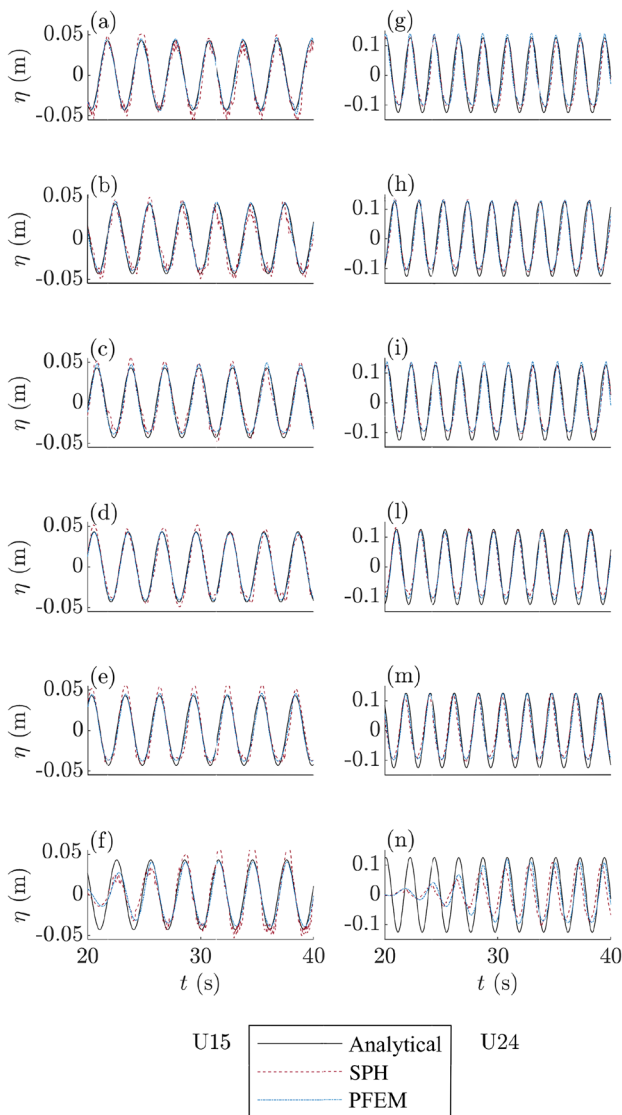


Fig. 11 Regular wave elevation at measurement gauges. Wave-type U15: left panels; wave-type U24: right panels. (a) (g) WGA, (b) (h) WGB, (c) (i) WGC, (d) (l) WGD, (e) (m) WGE, (f) (n) WGF

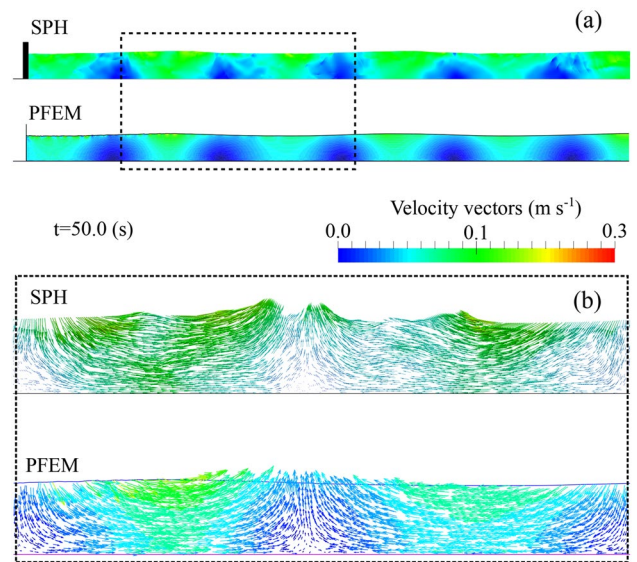


Fig. 12 Regular wave-type U15. **a** Magnitude velocity contours. **b** Velocity vectors

direction. In the node between the wave crest and the wave trough, the horizontal component of the velocity vector is null while the vertical component is directed upwards. Under the wave trough, the vertical velocity component is null and the horizontal velocity component is directed against the direction of wave propagation. The obtained results from both models are in accordance with the linear wave theory [33].

5.3 Non-linear wave-structure impact

The original laboratory experiment [52] was carried out in the flume at the hydraulic laboratory at the National University of Singapore. The freak wave was designed according to the focusing wave theory (13). $N = 32$ small amplitude waves meet simultaneously at a focusing point in space x_f and time t_f producing a large amplitude wave, which becomes a plunging breaker subsequently. This test case is applied here for the first time to the PFEM model and therefore used for validation.

$$\eta(x, t) = \sum_{i=1}^N a_i \cos[k_i(x - x_f) - 2\pi f_i(t - t_f)] \tag{13}$$

In Eq. (13), the index i refers to each linear wave component with a constant amplitude of $a_i = 0.0061m$. Frequency components f_i are equally spaced in the frequency bandwidth ranging from $f_{min} = 0.32Hz$ to $f_{max} = 0.96Hz$. The wave number k_i is computed for each linear wave component with the dispersion equation (linear theory). The characteristic wavelength is $L = 3.312m$ and the characteristic wave

celerity is $c = 2.11 \text{ ms}^{-1}$. The experimental velocity input for the wave-maker can be found in [20]. The adopted domain is shown in Fig. 13. The flat bottom is 16m long allowing the simulation of the non-linear wave at the focusing point $x_f = 11.104\text{m}$ (WG3). The wave is generated through a piston type wave-maker (left-hand boundary). A 1:10 sloped beach (right-hand side) prevents reflected waves. A 0.7m still water height is used and the wave elevation is recorded at three wave gauges WG1, WG2, and WG3. The bottom left corner of the fixed box-shaped structure is placed at $x = 12.677\text{m}$ and $y = 0.7458\text{m}$. Impact pressure time series are recorded at four probes, two on the bottom side and two on the front.

With the SPH, a resolution of $h/dx = 100$ is required to achieve accurate results for both the wave propagation and the fluid-solid impact. Instead, with the PFEM a coarser resolution would be sufficient to reproduce accurately the wave generation and propagation phenomena. However, a coarse discretisation would be not adequate to simulate satisfactorily the wave-structure impact. This is because contact elements connecting the solid obstacle and the free surface of the fluid at rest would be built during the PFEM remeshing. We remark that the distance between the water and the structure is less than 5cm. Therefore, for both SPH and PFEM models a resolution of $h/dx = 100$, i.e., a discretisation size of 0.007m is used. The adopted SPH artificial viscosity parameter $\alpha = 0.7$, is slightly higher than the one used in [20]. Table 4 shows the spatial resolution dx and the computational nodes/particles utilised for each model. It is worth noting that with the PFEM model a decreased simulation time can be achieved by adopting a variable mesh size with a consequent node number reduction.

Figure 14 shows the wave elevation at the three wave gauges. The models show similar results accurately reproducing the experimental wave elevation time series at each gauge. In Fig. 14 (c) the only difference between both

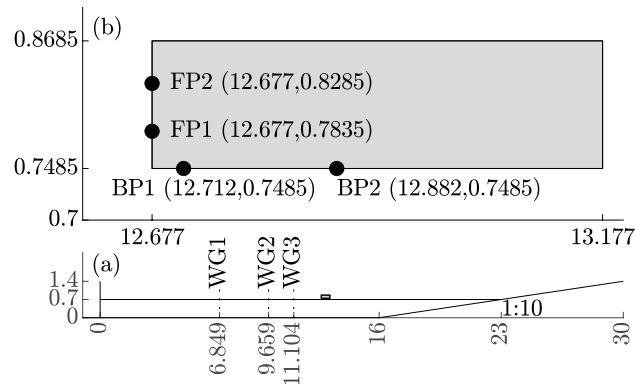


Fig. 13 Non-linear wave-structure impact. **a** Numerical flume. **b** Structure close-up. In this figure, all measures are in meters

Table 4 Simulation nodes - non-linear wave

dx (m)		End time (s)	N (-)	
SPH	PFEM		SPH	PFEM
0.007	0.007	20.00	278600	322764

models and the experimental wave elevation is at $t \approx 16.5\text{s}$. In this crest both numerical models show a reduced elevation with respect to the experimental data. However, the wave height at the subsequent crest ($t \approx 18.0\text{s}$) is more accurate. The PFEM model shows slightly higher accuracy than the SPH at some crests.

Figure 15 shows the impact pressures. At the front probes (Fig. 15 (a) and (b)) both models reproduce adequately the positive impact pressures. Peak values are similar to the experimental one for FP1 (Fig. 15 (a)) while they are slightly underestimated for FP2 (Fig. 15 (a)). The trend of the impact load is suitably reproduced by both models. At FP1 (Fig. 15 (a)) the SPH shows some secondary oscillations that are not shown in the results of the PFEM and the experiment. At FP2 (Fig. 15 (b)) the PFEM pressure time series is quite regular. At $t = 18.78\text{s}$, a secondary pressure increase is exhibited in the experimental signal that is well captured by the SPH model. Figure 15 (c) and (d) shows the bottom pressure probes. The positive impact pressures are well reproduced by both models even if the SPH overestimates the peaks. At the bottom probes, the SPH shows some oscillations as in the experimental signal but does not capture negative values. The PFEM model shows a regular trend with no oscillations and values close to the averaged

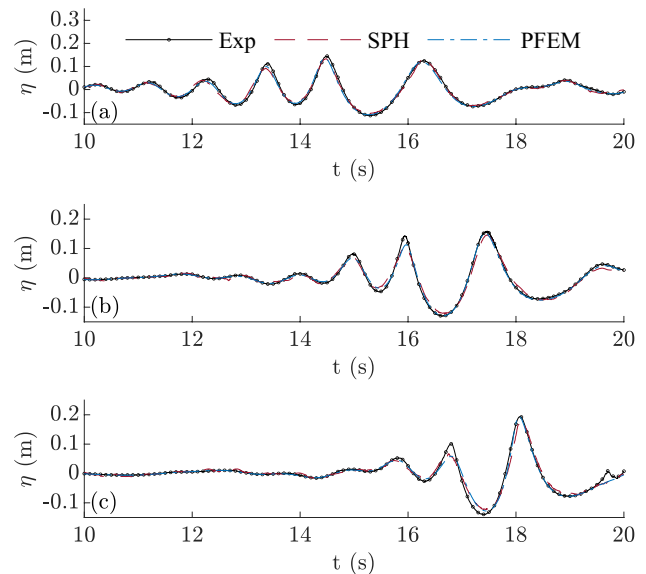


Fig. 14 Non-linear wave elevation at the gauges: **a** WG1, **b** WG2, **c** WG3

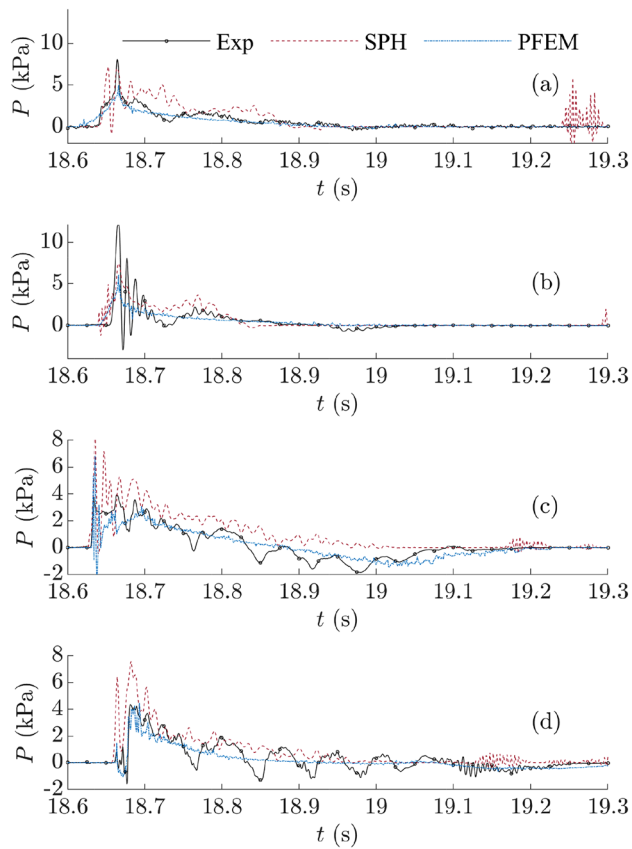


Fig. 15 Non-linear wave-structure impact pressure time series at the structure probes [52]. **a** FP1 **b** FP2 **c** BP1 **d** BP2

experimental signal. The time series of both models shows, on average, a similar trend to the experimental time series. At the bottom probes, the SPH computes slightly higher pressure values than the experiment and PFEM model. At BP1 (Fig. 15 (c)) from $t \approx 18.85$ s to $t \approx 19.1$ s strong suction pressures are recorded [53]. While the SPH model cannot capture these negative pressures due to tensile instability, the PFEM model reproduces the average suction pressures adequately. Similar considerations can be made for BP2 (Fig. 15 (d)). It is worth noting that other SPH models can reproduce the negative pressures [53] when the tensile instability is properly controlled.

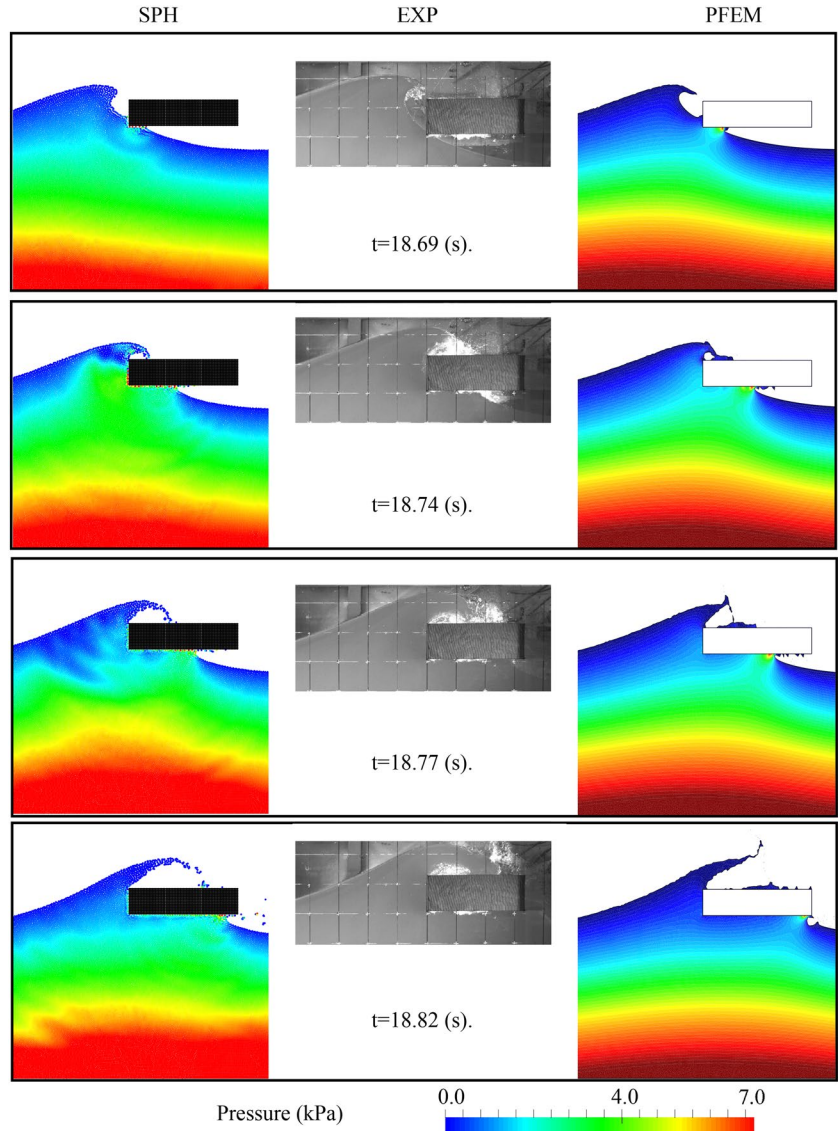
Figure 16 shows the pressure contours of the non-linear wave impact with the box shaped structure. The SPH and the PFEM results are shown on the left-hand and right-hand sides, respectively. In the centre, the experimental snapshots are given for comparison purposes. For each frame, pictures refer to the indicated time. The pressure contours produced by each model are quite similar. At $t = 18.69$ s, just before the impact, the pressure distribution is quasi-hydrostatic. On the bottom left corner of the structure, there is a slight pressure increase, with a similar magnitude for both models. Both models produce

a wave whose shape is similar to the experimental results. At $t = 18.74$ s, the SPH model produces higher pressure distribution around the wetted part of the structure than the PFEM, as shown in Fig. 15. In this frame the experimental wave is plunging onto the structure, this behaviour is captured by both models obtaining a similar behaviour. At $t = 18.77$ s, the PFEM pressure contour is smooth with the highest pressures around the bottom centre of the structure. The SPH shows pressure peaks in the same area, but there are some minor oscillations (owing to the fluid–structure boundary treatment). At this time the SPH wave is more similar to the experimental frame where the leading edge turns downwards. The PFEM model shows a different dynamics of the wavefront collapse. At $t = 18.82$ s, the SPH model produces slightly higher pressures to the bottom of the structure than PFEM model.

6 Conclusions

This work dealt with a comparative study among two Lagrangian particle-base numerical models, namely, SPH and PFEM, applied to the simulation of regular and non-linear waves in a flume with impact onto rigid structures. The analysed test cases were two solitary waves, two regular waves and a non-linear wave. Some of these test cases are investigated here for the first time and allow validation of the models. Results show that choosing the appropriate resolution, the wave elevation and the kinematic properties of the studied waves are adequately reproduced by both models. The PFEM wave elevation is not affected by relatively coarse mesh size. Instead, the SPH wave elevation is greatly improved with a higher spatial resolution. The SPH method needs a high number of neighbouring particles to obtain reliable results with the kernel approximation. The PFEM model instead is less influenced due to the FEM discretisation, which provides good results even for coarse resolutions. This aspect was highlighted in the analysis of solitary wave-type A where the influence of particle/mesh resolution was investigated. The non-linear wave impact result also shows that to model accurate impact pressures both models require a high spatial resolution. With higher resolution, both models can reproduce the pressure time history of the non-linear wave-structure impact. The SPH models slightly higher pressures than the experimental signal. The PFEM shows a regular trend with no oscillations and values close to the averaged experimental signal. Although the models are characterised by different Lagrangian approaches, they produce very similar results. The kinematic and dynamic properties of the analysed waves are reproduced adequately by both models and the achieved results are close to the experimental / analytical results of analysed waves. Given

Fig. 16 Non-linear wave-structure impact pressure contours. Left-hand column SPH, right-hand column PFEM. Comparison with experimental snapshots [52]



the appropriate parameter choice and mesh / particle sizes, both models can be considered validated to reproduce a wide range of waves.

Appendix A FEM discretization

In this appendix, we give the discretised form of the FIC-stabilised Navier-Stokes equations [28], briefly introduced in Sect. 4.1.

Let us consider a computational domain discretised into N_e finite elements with n nodes. For 2D problems, as those considered in this work, linear triangles are considered, therefore $n = 3$. Linear shape functions N_i^e are defined for each node i ($i = 1, n$) of the element e , both for the velocity

and the pressure field. [54–56]. Following the variational equation approach in [28], the governing equations (1a) and (1b) can be written in matrix form as

$$M_0 \dot{\mathbf{u}} + K \mathbf{u} + Q \bar{p} = \mathbf{f} \tag{A1}$$

$$M_1 \dot{\bar{p}} + M_2 \ddot{\bar{p}} + Q^T \mathbf{u} + (L + M_b) \bar{p} = \mathbf{f}_p \tag{A2}$$

The tensors of Eqs. (A1) and (A2) are defined as follows:

- $M_{0ij}^e = \int_{\Omega^e} \rho N_i^e N_j^e d\Omega$
- $K_{ij}^e = \int_{\Omega^e} \mathbf{B}_i^{eT} \mathbf{D} \mathbf{B}_j^e d\Omega$
- $Q_{ij}^e = \int_{\Omega^e} \mathbf{B}_i^{eT} \mathbf{m} N_j^e d\Omega$
- $M_{1ij}^e = \int_{\Omega^e} \frac{1}{k} N_i^e N_j^e d\Omega$

- $M_{2ij}^e = \int_{\Omega^e} \frac{\tau}{c^2} N_i^e N_j^e d\Omega$
- $M_{bij}^e = \int_{\Omega^e} \frac{2\tau}{h_n} N_i^e N_j^e d\Gamma$
- $L_{ij}^e = \int_{\Omega^e} \tau (\nabla^T N_i^e) \nabla N_j^e d\Omega$
- $f_i^e = \int_{\Omega^e} N_i^e \mathbf{b} d\Omega + \int_{\Gamma_i} N_i^e t d\Omega$
- $f_{pi}^e = \int_{\Gamma^i} \tau N_i^e [\rho \dot{u}_n - \frac{2}{h_n} (2\mu \epsilon_n - t_n)] d\Gamma - \int_{\Omega^e} \tau \nabla^T N_i^e \mathbf{b} d\Omega$

These integral are defined on the element domain Ω^e or at the frontier Γ^i . The sub-index n refers to the normal component, h is the mesh size, and the stabilisation parameter τ arising from the FIC procedure is defined as follows.

$$\tau = \left(\frac{8\mu}{h^2} + \frac{2\rho}{\delta} \right)^{-1} \tag{A3}$$

being h and δ a characteristic space and time lengths, respectively.

The tensors introduced in Eqs.(A1) and (A2) are listed below.

- $D = \mu \begin{pmatrix} 4/3 & -2/3 & 0 \\ -2/3 & 4/3 & 0 \\ 0 & 0 & 2 \end{pmatrix}$
- $B_i^e = \begin{pmatrix} \frac{\partial N_i}{\partial x} & 0 \\ 0 & \frac{\partial N_i}{\partial y} \\ \frac{\partial N_i}{\partial y} & \frac{\partial N_i}{\partial x} \end{pmatrix}$
- $N_i^e = N_i^e \mathbf{I}$
- $\nabla = \left(\frac{\partial}{\partial x}, \frac{\partial}{\partial y} \right)^T$
- $m = [1, 1, 0]^T$

Acknowledgements The authors would like to deeply thank Prof. Luo Min for his partial support for the Non-linear wave-structure impact test case. The EOS HPC cluster of the Department of Mathematics “Felice Casorati” at the University of Pavia is gratefully acknowledged. The authors acknowledge the contribution of the National Recovery and Resilience Plan, Mission 4 Component 2 - Investment 1.4 - NATIONAL CENTER FOR HPC, BIG DATA AND QUANTUM COMPUTING (project code: CN 00000013) - funded by the European Union - NextGenerationEU, as well as the support from the Italian Ministry of University and Research through the MIUR-PRIN project “XFAST-SIMS” (no. 20173C478N).

Author Contributions NS Conceptualisation, Software, Simulations, Validation, Writing-Original Draft. AF Conceptualisation, Software, Writing-Review, Supervision. SI Writing-Review & Editing AR Conceptualisation, Writing-Review & Editing SM Conceptualisation, Writing-Original Draft, Supervision.

Funding Open access funding provided by Università degli Studi di Pavia within the CRUI-CARE Agreement. The partial support by the MIUR-PRIN project XFAST-SIMS (no. 20173C478N) is gratefully acknowledged.

Code availability SPHERA v.9.0.0 derived model https://github.com/ncsalis/SPHERA/tree/SPHERA_v_9_0_0_NS_2P Kratos <https://github.com/KratosMultiphysics/KratosGiD> <https://github.com/ncsalis/GiDIn> interface.

Declarations

Conflict of interest The authors declare that they have no known competing financial interests or personal relationships that could have appeared to influence the work reported in this paper.

Open Access This article is licensed under a Creative Commons Attribution 4.0 International License, which permits use, sharing, adaptation, distribution and reproduction in any medium or format, as long as you give appropriate credit to the original author(s) and the source, provide a link to the Creative Commons licence, and indicate if changes were made. The images or other third party material in this article are included in the article’s Creative Commons licence, unless indicated otherwise in a credit line to the material. If material is not included in the article’s Creative Commons licence and your intended use is not permitted by statutory regulation or exceeds the permitted use, you will need to obtain permission directly from the copyright holder. To view a copy of this licence, visit <http://creativecommons.org/licenses/by/4.0/>.

References

1. Huang C-J, Zhang E-C, Lee J-F (1998) Numerical simulation of nonlinear viscous wavefields generated by piston-type wave-maker. *J Eng Mech* 124(10):1110–1120
2. Anbarsooz M, Passandideh-Fard M, Moghiman M (2013) Fully nonlinear viscous wave generation in numerical wave tanks. *Ocean Eng* 59:73–85
3. Mohapatra SC, Islam H, Hallak TS, Soares CG (2022) Solitary wave interaction with a floating pontoon based on boussinesq model and cfd-based simulations. *J Mar Sci Eng* 10(9):1251
4. Yan M, Ma X, Bai W, Lin Z, Li Y (2020) Numerical simulation of wave interaction with payloads of different postures using openfoam. *J Mar Sci Eng* 8(6):433
5. Pákozdi C, Östeman A, Stansberg CT, Peric M, Lu H, Baarholm R (2015) Estimation of wave in deck load using cfd validated against model test data. In: *The Twenty-fifth International Ocean and Polar Engineering Conference*. OnePetro
6. Stansberg CT, Baarholm R, Kristiansen T, Hansen E, Rortveit G (2005) Extreme wave amplification and impact loads on offshore structures. In: *Offshore Technology Conference*. OnePetro
7. Lucy LB (1977) A numerical approach to the testing of the fission hypothesis. *Astron J* 82:1013–1024
8. Sulsky D, Chen Z, Schreyer HL (1994) A particle method for history-dependent materials. *Comput Methods Appl Mech Eng* 118(1–2):179–196. [https://doi.org/10.1016/0045-7825\(94\)90112-0](https://doi.org/10.1016/0045-7825(94)90112-0)
9. Idelsohn SR, Nigro N, Gimenez J, Rossi R, Marti J (2013) A fast and accurate method to solve the incompressible navier-stokes equations. *Eng Comput* 30(3):197–222
10. Idelsohn SR, Oñate E, Pin FD (2004) The particle finite element method: a powerful tool to solve incompressible flows with free-surfaces and breaking waves. *Int J Numer Meth Eng* 61(7):964–989
11. Gingold RA, Monaghan JJ (1977) Smoothed particle hydrodynamics: theory and application to non-spherical stars. *Mon Not R Astron Soc* 181(3):375–389
12. Monaghan JJ (1994) Simulating free surface flows with sph. *J Comput Phys* 110(2):399–406

13. Monaghan J, Kocharyan A (1995) Sph simulation of multi-phase flow. *Comput Phys Commun* 87(1–2):225–235
14. Koshizuka S, Oka Y (1996) Moving-particle semi-implicit method for fragmentation of incompressible fluid. *Nucl Sci Eng* 123(3):421–434
15. Koh C, Gao M, Luo C (2012) A new particle method for simulation of incompressible free surface flow problems. *Int J Numer Meth Eng* 89(12):1582–1604
16. Lind SJ, Xu R, Stansby PK, Rogers BD (2012) Incompressible smoothed particle hydrodynamics for free-surface flows: A generalised diffusion-based algorithm for stability and validations for impulsive flows and propagating waves. *J Comput Phys* 231(4):1499–1523
17. Liu X, Lin P, Shao S (2015) Isph wave simulation by using an internal wave maker. *Coast Eng* 95:160–170
18. Altomare C, Tafuni A, Domínguez JM, Crespo AJ, Gironella X, Sospedra J (2020) Sph simulations of real sea waves impacting a large-scale structure. *J Mar Sci Eng* 8(10):826
19. Salis N, Luo M, Reali A, Manenti S (2021) Sph simulation of water waves and impact with a rigid offshore structure in a 2d flume. In: *The 31st International Ocean and Polar Engineering Conference*. OnePetro
20. Salis N, Luo M, Reali A, Manenti S (2022) Wave generation and wave-structure impact modelling with wcsph. *Ocean Eng* 266:113228. <https://doi.org/10.1016/j.oceaneng.2022.113228>
21. Luo M, Reeve DE, Shao S, Karunarathna H, Lin P, Cai H (2019) Consistent particle method simulation of solitary wave impinging on and overtopping a seawall. *Eng Anal Bound Elem* 103:160–171
22. Oñate E, Idelsohn SR, Del Pin F, Aubry R (2004) The particle finite element method. an overview. *Int J Comput Methods* 2:267–307. <https://doi.org/10.1142/S0219876204000204>
23. Oliveira T, Sánchez-Arcilla A, Gironella X (2012) Simulation of wave overtopping of maritime structures in a numerical wave flume. *J Appl Math*. <https://doi.org/10.1155/2012/246146>
24. Oliveira TCA, Sanchez-Arcilla A, Gironella X, Madsen OS (2017) On the generation of regular long waves in numerical wave flumes based on the particle finite element method. *J Hydraul Res* 55(4):538–556. <https://doi.org/10.1080/00221686.2016.1275047>
25. Mulligan R, Franci A, Celigueta M, Take W (2020) Simulations of landslide wave generation and propagation using the particle finite element method. *J Geophys Res Oceans* 125:2019–015873. <https://doi.org/10.1029/2019JC015873>
26. Oñate E, Cornejo A, Zárate F, Kashiyama K, Franci A (2022) Combination of the finite element method and particle-based methods for predicting the failure of reinforced concrete structures under extreme water forces. *Eng Struct* 251:113510
27. Franci A, Masó M, Cornejo A (2022) A lagrangian-eulerian procedure for the coupled solution of the navier-stokes and shallow water equations for landslide-generated waves. *Adv Model Simul Eng Sci* 9(1):15
28. Oñate E, Franci A, Carbonell JM (2014) Lagrangian formulation for finite element analysis of quasi-incompressible fluids with reduced mass losses. *Int J Numer Meth Fluids* 74(10):699–731
29. Cremonesi M, Franci A, Idelsohn S, Oñate E (2020) A state of the art review of the particle finite element method (pfem). *Arch Comput Methods Eng* 27(5):1709–1735
30. Meduri S, Cremonesi M, Perego U (2019) An efficient runtime mesh smoothing technique for 3d explicit lagrangian free-surface fluid flow simulations. *Int J Numer Meth Eng* 117(4):430–452
31. SPHERA (RSE SpA) (2023) <https://github.com/GiordanoAgateRSE/SPHERA>
32. KratosMultiphysics (2022) <https://github.com/KratosMultiphysics/Kratos>
33. Dean RG, Dalrymple RA (1991) *Water wave mechanics for engineers and scientists*, vol 2. World scientific publishing company
34. “Derived code” (2022) https://github.com/ncsalis/SPHERA/tree/SPHERA_v_9_0_0_NS_2P
35. Amicarelli A, Marongiu J-C, Leboeuf F, Leduc J, Neuhauser M, Fang L, Caro J (2011) Sph truncation error in estimating a 3d derivative. *Int J Numer Meth Eng* 87(7):677–700
36. Di Monaco A, Manenti S, Gallati M, Sibilla S, Agate G, Guandalini R (2011) Sph modeling of solid boundaries through a semi-analytic approach. *Eng Appl Comput Fluid Mech* 5(1):1–15
37. Amicarelli A, Albano R, Mirauda D, Agate G, Sole A, Guandalini R (2015) A smoothed particle hydrodynamics model for 3d solid body transport in free surface flows. *Comput Fluids* 116:205–228
38. Amicarelli A, Manenti S, Albano R, Agate G, Paggi M, Longoni L, Mirauda D, Ziane L, Viccione G, Todeschini S et al (2020) Sphera v. 9.0. 0: A computational fluid dynamics research code, based on the smoothed particle hydrodynamics mesh-less method. *Comput Phys Commun* 250:107157
39. Antuono M, Colagrossi A, Marrone S (2012) Numerical diffusive terms in weakly-compressible sph schemes. *Comput Phys Commun* 183(12):2570–2580
40. Adami S, Hu XY, Adams NA (2012) A generalized wall boundary condition for smoothed particle hydrodynamics. *J Comput Phys* 231(21):7057–7075
41. Manenti S, Sibilla S, Gallati M, Agate G, Guandalini R (2012) Sph simulation of sediment flushing induced by a rapid water flow. *J Hydraul Eng* 138(3):272–284
42. Monaghan JJ (2005) Smoothed particle hydrodynamics. *Rep Prog Phys* 68(8):1703
43. Brezzi F, Fortin M (1991) *Mixed and hybrid finite element methods*. Springer, New York
44. Edelsbrunner H, Tan TS (1993) An upper bound for conforming delaunay triangulations. *Discret Comput Geom* 10(2):197–213
45. Edelsbrunner H, Mücke EP (1999) Three dimensional alpha shapes. *ACM Trans Graph(TOG)* 13(1):43–72
46. Arikawa T (2009) Structural behavior under impulsive tsunami loading. *J Disaster Res* 4(6):377–381
47. Krautwald C, Stolle J, Hitzegrad J, Niebuhr P, Goseberg N, Nistor I, Sieder M (2020) Large-scale physical modelling of a broken solitary wave impact on rigid and non-rigid box-like structures. *Coast Eng Proceed*. <https://doi.org/10.9753/icce.v36v.structures.19>
48. Krautwald C, Stolle J, Robertson I, Achiari H, Mikami T, Nakamura R, Takabatake T, Nishida Y, Shibayama T, Esteban M et al (2021) Engineering lessons from september 28, 2018 indonesian tsunami: Scouring mechanisms and effects on infrastructure. *J Waterw Port Coast Ocean Eng* 147(2):04020056
49. Krautwald C, Von Häfen H, Niebuhr P, Vögele K, Schürenkamp D, Sieder M, Goseberg N (2022) Large-scale physical modeling of broken solitary waves impacting elevated coastal structures. *Coast Eng J* 64(1):169–189
50. Biésel F, Suquet F (1951) *Les appareils générateurs de houle en laboratoire*. La houille blanche
51. Ursell F, Dean RG, Yu Y (1960) Forced small-amplitude water waves: a comparison of theory and experiment. *J Fluid Mech* 7(1):33–52
52. Yan B, Luo M, Bai W (2019) An experimental and numerical study of plunging wave impact on a box-shape structure. *Mar Struct* 66:272–287
53. Sun P-N, Luo M, Le Touzé D, Zhang A-M (2019) The suction effect during freak wave slamming on a fixed platform deck: Smoothed particle hydrodynamics simulation and experimental study. *Phys Fluids* 31(11):117108
54. Zienkiewicz, O.C., Taylor, R.L.: *The finite element method*, volume i. Fluid dynamics (2000)
55. Oñate E (2013) *Structural Analysis with the Finite Element Method*. Linear Statics: Volume 2: Beams, Plates and Shells. Springer,

56. Zienkiewicz OC, Taylor RL, Zhu JZ (2005) The finite element method: its basis and fundamentals. Elsevier

Publisher's Note Springer Nature remains neutral with regard to jurisdictional claims in published maps and institutional affiliations.